Medial Tractography Analysis (MeTA) for White Matter Population Analyses Across Datasets

Iyad Ba Gari[1], Abhinaav Ramesh[1], Shayan Javid[1], Shruti P. Gadewar[1], Elnaz Nourollahimoghadam[1], Sophia I. Thomopoulos[1], Paul M. Thompson[1], Talia M. Nir[1], Neda Jahanshad[1], for the Alzheimer's Disease Neuroimaging Initiative

2023 11th International IEEE/EMBS Conference on Neural Engineering (NER) | 978-1-6654-6292-1/23/$31.00 ©2023 IEEE | DOI: 10.1109/NER52421.2023.10123727

***Abstract*— Diffusion MRI tractography can be used to study the structural connections of the human brain. It allows us to quantify the shape and connectivity of white matter (WM) bundles (tracts) in a noninvasive way that helps us to investigate brain function and disease. Various protocols and techniques have been implemented to segment WM tractograms, but different acquisition protocols and processing pipelines lead to unwanted methodological variation in the size, shape, and densities of the segmented tracts. As the neuroimaging field moves towards large-scale multi-site analyses, multi-site diffusion MRI analyses have largely focused on metric derived from scalar maps, such as tract-based spatial statistics (TBSS) as opposed to using the rich information available in 3D tractograms. Here we propose Medial Tractography Analysis (MeTA)- a novel approach that extends current state of the art medial curve methods for bundle analysis. MeTA offers a medial core volume to allow for quantitative bundle analyses that retain key information on bundle shape, and reduce the influence of partial voluming in analyzing tract-wise microstructural properties. Compared to TBSS- a voxel-based approach to study the WM core- we found that the tractography-based MeTA approach improved detection sensitivity for associations between Alzheimer's disease biomarkers such as amyloid (Aβ) and tau load and hippocampal-cingulum DTI fractional anisotropy and mean diffusivity.**

I. Introduction

Diffusion-weighted magnetic resonance imaging (dMRI) can be used to reveal trajectories of the brain's white matter (WM) pathways. Variation in these pathways can shed light on numerous aspects of brain development, aging, and various neuropsychiatric disorders across the lifespan. To study specific WM connections, full brain tractograms can be segmented into specific WM tracts, or pathways. Many tract segmentation tools exist [1-7]. Once specific bundles are extracted, population analyses of WM tracts can be performed to understand the normal variations in brain connectivity and abnormal alterations with disease progression.

Population-based analyses include analyses of WM microstructure within the bundle, along the bundle, or analyses of the shape of the bundle itself [3]. For example, BUndle ANalytics (BUAN) is a tool that, among other processes, parameterizes the full bundle volume for population statistics [8]. Similarly, CM-Rep can represent the WM tracts by a parametric surface and can perform manifold-based statistical analyses [9].

[1] Imaging Genetics Center, Mark and Mary Stevens Neuroimaging and Informatics Institute, Keck School of Medicine, University of Southern California, Marina del Rey, CA, USA. bagari@usc.edu & njahansh@usc.edu

These methods require tracts to be aligned across individuals, and this mapping can often be compromised due to variation in WM bundle shapes and partial voluming with the adjacent gray matter. While these effects are often relatively uniform within specific studies, affecting all individuals in a study population, whole brain tractography and parsed bundles are often noisy and include many spurious streamlines. The quality of the tractography and bundle segmentation can also be highly dependent on dMRI acquisition parameters [10] and preprocessing steps [11].

The neuroimaging field is moving towards larger scale, multi-site studies that pool data across various institutions, collected at different times, and using a variety of protocols [12]. Compatibility of tractography bundles is needed not only within a specific dataset, but across datasets. To date, most multi-site analyses of WM have been limited to the analysis of scalar microstructure maps themselves, as opposed to analyses of the fiber bundles.

One of the most common tools for multi-site WM analysis is tract-based spatial statistics (TBSS) [13]; dMRI measures from voxels with the highest anisotropy (tract-center) are projected onto a WM skeleton. This method avoids issues such as partial voluming along the gray and white matter boundaries, minimizes issues related to misregistration across multiple subjects, and is a widely-used method for multi-site, multi-cohort analyses of WM microstructure from scalar images, such as those conducted by large-scale consortia [14]. Even so, TBSS limits analyses to the WM skeleton and lacks the anatomical specificity and fine-scale resolution of tractography-based methods.

Here, we extend the TBSS concept of analyzing core WM tracts to improve consistency in multi-site studies to tractography. We build on CM-Reps [9] to develop Medial Tractography Analysis (MeTA) - a novel tool to reduce the microstructural heterogeneity and variability of dMRI metrics within bundles extracted using existing tract segmentation tools. Rather than simply extracting a central medial curve [15], we aim to provide a central volume - which enables us to extract bundle-level shape features on a central volume defined geometrically around a medial surface. We use test-retest data and multi-protocol data from the Alzheimer's Disease Neuroimaging Initiative to show that our method: 1) works on bundles derived from multiple bundle segmentation schemes (TractSeg [3] and DSI-Studio [5]), 2) allows users to extract reliable bundle-wise metrics (with high test-retest reliability).

and 3) can detect more robust associations with clinical measures than TBSS, in a multi-site study.

II. METHODS

A. Medial Surface and Core Extraction

For a 3D object **X**, a CM-Rep (**m**) is a continuous medial surface with a radius scalar field (**R**) on the surface [9]. The boundary generated of **X** objects is constructed using a maximum inscribed ball (**MIB**) of radius **R** at each point on the medial surface (**m**). Object **X** can be described as $X^{\pm}$ which is on opposite sides of the medial surface (**m**). $X^{\pm}$ may be considered as the points of tangency between X and the **MIB** of **m** with radius **R**.

$$\mathrm{X}^{\pm} = \mathrm{m} + \mathrm{R}\mathrm{U}^{\pm} \tag{1}$$

Here $U^{\pm}$ are the unit outward normal vectors on both directions of **X**

$$\mathrm{U}^{\pm} = -\nabla_{\mathrm{m}}\mathrm{R} \pm \sqrt{1 - |\nabla_{\mathrm{m}}\mathrm{R}|^2}\,\mathrm{N}_{\mathrm{m}} \tag{2}$$

where $N_m$is the unit normal of the medial surface, and $\nabla_m R$ is the gradient of scalar radius R on the medial surface.

We then used the medial surface (**m**) and boundary mesh **X** to compute the central 25% of the mesh by computing the 37.5% and 62.5% surfaces using ray tracing methods [16]. We calculated the normal on the vertex points of the medial surface (**m**), and then traveling along the surface normal in both directions ($X^{\pm}$) to reach the outer boundary mesh points.

We used a KD-Tree [17] to compute the distance from every vertex point in the medial surface X to its closest vertex point on the outer boundary mesh that lies on the normal axis in both directions. Finally, we calculated the shortest distance (thickness/depth) from the vertex point on the medial surface to the boundary mesh. The new computed points on both sides of the medial surface are used to get the sub-volume from the original boundary.

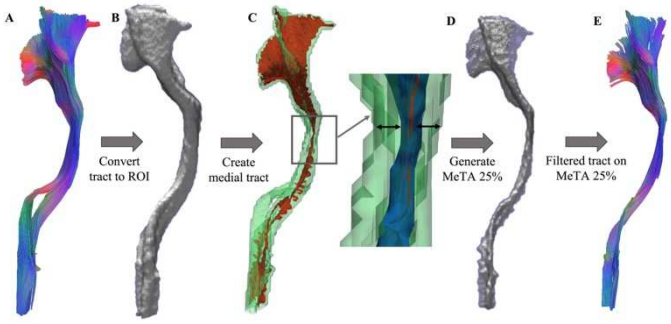

Fig. 1. **Medial surface and core extraction workflow. A.** The generated white matter bundle from TractSeg is **B.** converted to a volume of interest. **C.** *Green color* shows the constructed boundary object, whereas the *red color* represents the medial surface of the object. The *black arrows* show the distance between 37.5% and 62.5% surfaces, *in blue*, from the object's boundary. **D.** Voxelized MeTA_25% using the computed depth from medial surface using the ray tracing method. **E.** Filtered streamlines of the tracts contained in the MeTA 25% volume.

B. Datasets

We used the WU-Minn HCP [18] and Penthera3T datasets [19] in our test-retest analysis (Table I). dMRI images from the Penthera (PT) dataset were denoised using Local PCA [20], deGibbs [21], corrected for eddy current and motion artifacts (using FSL eddy [22]). The preprocessed version of the WU-Minn HCP was downloaded.

TABLE I. DEMOGRAPHIC DETAILS FOR TEST-RETEST DATASETS

Dataset	Age range	N (F)	Voxel size $(mm)^3$	N(Volume)	b-value (mm^2/s)
HCP	22-35	32 (23)	1.25x1.25.1 25	90,90,90	1000,2000, 3000
Penthera	24-30	11(3)	2x2x2	8,32,60	300,1000, 2000

We used a multi-shell, multi-tissue constrained spherical deconvolution method [23] to extract probabilistic tractography (iFOD2) for the whole brain. Six major WM bundles were segmented from tractograms using the TractSeg tool [5]: the arcuate fasciculus (AF), cingulum (CG), corticospinal tract (CST), inferior fronto-occipital fasciculus (IFO), inferior longitudinal fasciculus (ILF), and uncinate fasciculus (UF). Within each extracted bundle, we calculated the medial surface using CM-Rep [9], and implemented a new method to extract the medial core volume, which encloses the central 25% volume, 12.5% of the total volume from each side of the medial surface; we will refer to this volume as MeTA_25%.

C. Reliability Statistics

We computed the median and the median absolute deviation (MAD) of the DTI fractional anisotropy (FA) and mean diffusivity (MD) measures within each of the 6 tracts. The intraclass correlation (ICC) was calculated using Pingouin in Python [24]. We assessed test-retest reliability of dMRI metrics, in each of the full TractSeg ('all', i.e., 100%), and the further reduced MeTA_25% (37.5-62.5) masks. We used the mean of k raters of ICC2 to remove the mean difference between scan sessions and considered the random effect [25]:

$$\mathrm{ICC2} = \frac{\mathrm{BMS}-\mathrm{EMS}}{(\mathrm{BMS}+(\mathrm{k}-1)\mathrm{EMS}+\mathrm{k}(\mathrm{JMS}-\mathrm{EMS})/\mathrm{n}'} \tag{3}$$

Here, BMS is the between-targets mean square (subjects), EMS is the residual mean square, k is the number of judges (2 scan sessions) rating each target, JMS is the between-judges (scan sessions) mean square, and n' is the number of targets (subjects). We quantified the DTI microstructural variation in each tract between subjects using the median absolute deviation (MAD) for one scan session and performed *t*-tests between all vs MeTA_25% masks for each tract.

D. Clinical application

The greatest WM microstructural differences between individuals with dementia and cognitively unimpaired controls (CN) have previously been reported in the parahippocampal cingulum [26]. To demonstrate flexibility in our approach across bundle segmentation algorithms, we segmented the parahippocampal cingulum (C_PH) using DSI-Studio [3] from the ADNI3 dMRI data, which was collected with seven different protocols. We then extracted MeTA_25% and compared median DTI FA and MD diffusion metrics between mild cognitive impairment (MCI) and CN ADNI3 participants (Table II), using linear mixed-effects models adjusting for age, sex, and scan site as a random variable. We investigated differences associated with the Montreal Cognitive Assessment (MoCA), Mini-Mental State Examination (MMSE), and Clinical Dementia Rating

Scale Sum of Boxes (CDR-SB), as well as amyloid (Aβ) and tau load indexed with FBB/FBP or AV-1451 positron emission tomography, respectively. Cortical Aβ and temporal tau SUVRs were binarized using cut-points defined in [27].

TABLE II. DEMOGRAPHIC AND CLINICAL MEASURES FOR PARTICIPANTS IN THE ADNI3 DATASET, SPLIT BY DMRI PROTOCOL

Protocols	N	Age (yrs)	N (Female)	CN (MCI)	$A\beta^-$ ($A\beta^+$)	tau^- (tau^+)
P33	56	75.7±7.7	22	37 (14)	19 (21)	26 (11)
P36	46	73.1±6.9	22	20 (23)	24 (15)	22 (15)
S31	96	72±8.5	57	59 (27)	49 (28)	56 (21)
S55	260	74.4±7.8	143	169 (68)	103 (116)	135 (66)
S127	109	73.8±7.6	57	66 (35)	55 (36)	66 (20)
GE36	41	72.2±7.22	17	21 (16)	20 (14)	25 (9)
GE54	106	76.2±8.11	52	65 (26)	50 (42)	62 (23)
Total	714	74.2±7.9	370	437 (209)	320 (272)	392 (165)

III. RESULTS

A. Diffusion microstructure reliability

Overall, intraclass correlation of FA and MD for both the Penthera and HCP datasets were moderate to highly reliable across all tracts for both the full bundle (‘all’) and the MeTA_25%. We note slight improvements in ICC with the MeTA_25% in most cases where the full bundle (‘all’) was less reliable (ICC < 0.75), but this was not significant due to the overall high reliability. The reliability across all tracts of the Penthera dataset was high (average ICCk=0.939 ± 0.037), regardless of method.

TABLE III. FA AND MD ICC2K TEST-RETEST ESTIMATES ACROSS 6 LATERALIZED TRACTS FOR ALL AND META_25% ON HCP AND PT DATASETS.

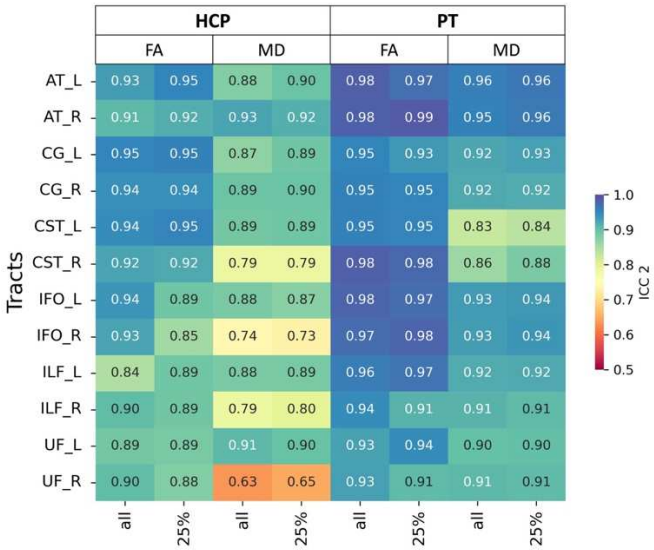

B. Subjects’ variation across scan sessions

The overall median value of all tracts is plotted in Figure 2. In the HCP, we found significant differences in FA MAD between the MeTA_25% core mask and “all” mask in AF, CG, CST, IFO, and UF, bilaterally. Similarly, in the Penthera dataset, we found significant differences in the AF_L, CG_L, CG_R, CST_L, and CST_R. We also found a significant MD difference between MeTA_25% and “all” in CST_L, CST_R, IFO_R. Similar trends were detected in Penthera (Figure 2).

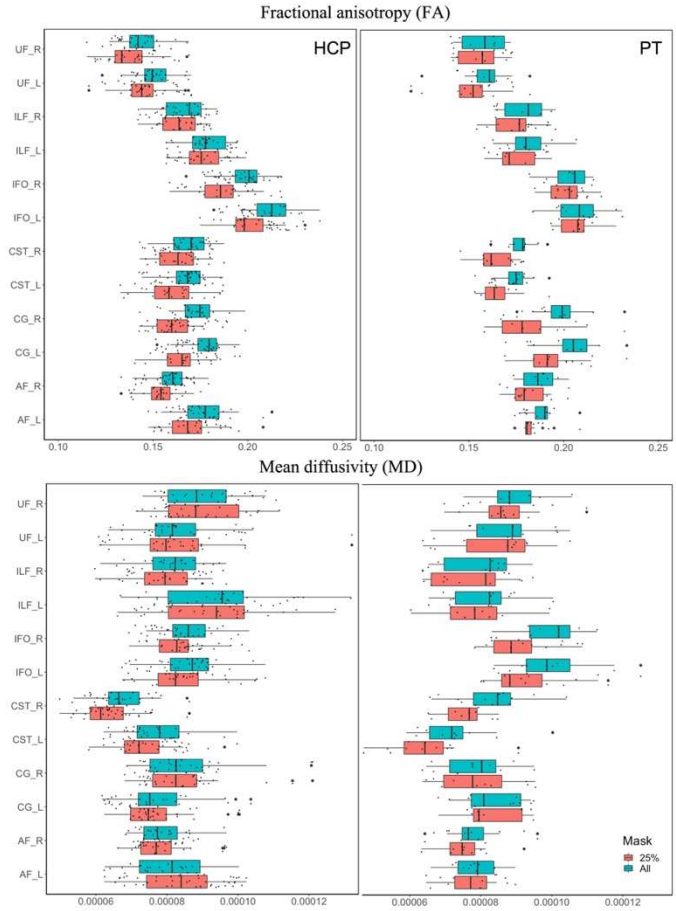

Fig. 2. Within subject variation of diffusion microstructure metrics for HCP and PT datasets. The cyan color represents measures extracted from the full TractSeg bundle mask (‘all’), while the red represents measures within the MeTA mask (25%).

C. Protocol effects on dMRI metrics in ADNI

As shown in Figure 3, across ADNI protocols, while TBSS had the lowest FA and MD residual variation, compared to the whole tract (‘all’), MeTA_25% had lower residual variation.

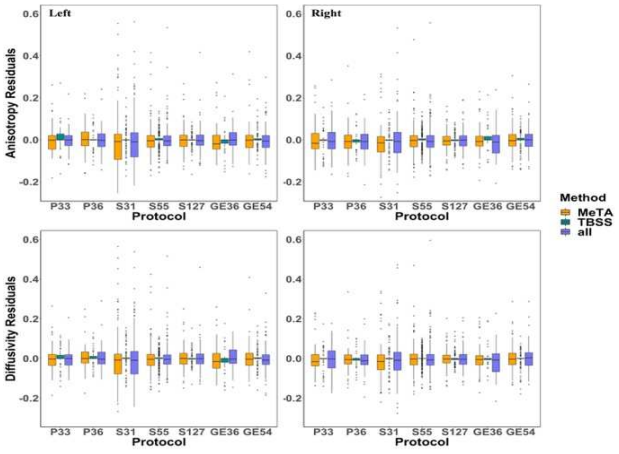

Fig. 3. TBSS, MeTA, and whole tract (‘all’) MD and FAresiduals in the left and right parahippocampal cingulum for each ADNI3 protocol, after adjusting for age and sex.

D. ADNI association

As shown in Table IV, the MeTA_25% C_PH DTI measures were more strongly associated with both cognitive assessments as well as Aβ and tau pathology compared to TBSS, highlighting that the additional variability observed in Figure 3 was biologically meaningful. In fact, amyloid associations were only detectable with MeTA.

TABLE IV. USING META, DTI MEASURES IN THE LEFT AND RIGHT PARAHIPPOCAMPAL CINGULUM WERE SIGNIFICANTLY DIFFERENT BETWEEN GROUPS OF INDIVIDUALS WITH A) MCI VS CN, B) PET-DEFINED BETA AMYLOID POSITIVITY *VS.* NOT, OR C) PET-DEFINED TAU POSITIVITY *VS.* NOT, AND ASSOCIATED WITH CDR-SB, MOCA, AND MMSE

C_PH	Group	Tool	FA		MD	
			r	p	r	p
L	CN vs MCI	MeTA	-0.15	1.92×10^{-4}	0.24	5.56×10^{-9}
		TBSS	-0.13	1.21×10^{-3}	0.14	7.14×10^{-4}
	$A\beta^-$ vs $A\beta^+$	MeTA	-0.07	0.12	0.15	5.79×10^{-4}
		TBSS	-0.08	0.068	0.10	0.025
	TAU- vs TAU+	MeTA	-0.16	4.99×10^{-4}	0.29	3.24×10^{-11}
		TBSS	-0.21	1.36×10^{-6}	0.22	2.29×10^{-7}
	CDRSB	MeTA	-0.29	7.32×10^{-14}	0.50	2.14×10^{-42}
		TBSS	-0.32	5.67×10^{-17}	0.32	1.9×10^{-16}
	MoCA	MeTA	0.18	2.02x10-^{5}	-0.42	1.11×10^{-25}
		TBSS	0.23	2.65×10^{-8}	-0.26	1.19×10^{-10}
	MMSE	MeTA	0.23	1.81×10^{-9}	-0.45	1.5×10^{-32}
		TBSS	0.26	3.5×10^{-11}	-0.28	1.14×10^{-12}
R	CN vs MCI	MeTA	-0.13	1.38×10^{-3}	0.19	4.19×10^{-6}
		TBSS	-0.07	0.08	0.14	6.42×10^{-4}
	$A\beta^-$ vs $A\beta^+$	MeTA	-0.10	0.017	0.16	1.61×10^{-4}
		TBSS	-0.14	1.03×10^{-3}	0.09	0.036
	TAU- vs TAU+	MeTA	-0.22	1.06×10^{-6}	0.31	1.59×10^{-12}
		TBSS	-0.21	1.51×10^{-6}	0.23	2.74×10^{-7}
	CDRSB	MeTA	-0.29	1.63×10^{-13}	0.47	2.0×10^{-36}
		TBSS	-0.28	4.36×10^{-13}	0.28	7.16×10^{-13}
	MoCA	MeTA	0.24	7.55×10^{-9}	-0.40	6.85×10^{-24}
		TBSS	0.23	2.44×10^{-8}	-0.23	2.06×10^{-8}
	MMSE	MeTA	0.26	3.69×10^{-11}	-0.43	8.3×10^{-30}
		TBSS	0.25	1.36×10^{-10}	-0.26	1.33×10^{-11}

IV. DISCUSSION

We extended the CM-Rep approach to develop MeTA, which reduces the microstructural heterogeneity and variability within the bundle. We found higher FA and MD ICC values with MeTA_25% masks in test-retest datasets compared to the whole tract('all'). While the variance in DTI measures was greater in MeTA tracts than in the TBSS ROIs, we found stronger MeTA associations with AD-related clinical and pathological measures in multi-site, multi-protocol ADNI3 dMRI data. This suggests that bundle analyses based on MeTA may help to identify more subtle effects that may be underestimated or even missed using a WM skeleton based on voxel-wise FA. The MeTA approach also focuses on sets of streamlines that have more homogeneous microstructure than the full bundle ('all'), as we showed, with lower variability. Future work will include parameterization of the core bundles for along-tract statistical analyses.

ACKNOWLEDGMENT

This research was supported by NIH grants P41EB015922, R01AG059874, RF1AG057892, and R01MH11760. Data were provided [in part] by the Human Connectome Project, WU-Minn Consortium (Principal Investigators: David van Essen and Kamil Ugurbil; U54MH091657) funded by the 16 NIH Institutes and Centers that support the NIH Blueprint for Neuroscience Research; and by the McDonnell Center for Systems Neuroscience at Washington University. Alzheimer's Disease Neuroimaging Initiative (ADNI) database (adni.loni.usc.edu). As such, the investigators within the ADNI contributed to the design and implementation of ADNI and/or provided data but did not participate in analysis or writing of this report. A complete listing of ADNI investigators can be found at: http://adni.loni.usc.edu/wp-content/uploads/how_to_apply/ADNI_Acknowledgement_List.pdf.

REFERENCES

[1] A. Yendiki *et al.*, "Automated probabilistic reconstruction of white-matter pathways in health and disease using an atlas of the underlying anatomy," *Front. Neuroinform.*, vol. 5, p. 23, Oct. 2011.

[2] D. Wassermann *et al.*, "The white matter query language: a novel approach for describing human white matter anatomy," *Brain Struct. Funct.*, vol. 221, no. 9, pp. 4705–4721, Dec. 2016.

[3] F.-C. Yeh, "Shape analysis of the human association pathways," *Neuroimage*, vol. 223, p. 117329, Dec. 2020.

[4] V. Siless, K. Chang, B. Fischl, and A. Yendiki, "AnatomiCuts: Hierarchical clustering of tractography streamlines based on anatomical similarity," *Neuroimage*, vol. 166, pp. 32–45, Feb. 2018.

[5] J. Wasserthal, P. Neher, and K. H. Maier-Hein, "TractSeg - Fast and accurate white matter tract segmentation," *Neuroimage*, vol. 183, pp. 239–253, Dec. 2018.

[6] V. Gupta, S. I. Thomopoulos, F. M. Rashid, and P. M. Thompson, "FiberNET: An ensemble deep learning framework for clustering white matter fibers," *bioRxiv*, p. 141036, 24-May-2017.

[7] Y. Jin *et al.*, "Automatic clustering of white matter fibers in brain diffusion MRI with an application to genetics," *Neuroimage*, vol. 100, pp. 75–90, Oct. 2014.

[8] B. Q. Chandio *et al.*, "Bundle analytics, a computational framework for investigating the shapes and profiles of brain pathways across populations," *Sci. Rep.*, vol. 10, no. 1, p. 17149, Oct. 2020.

[9] P. A. Yushkevich, H. Zhang, and J. C. Gee, "Continuous medial representation for anatomical structures," IEEE Trans. Med. Imaging, vol. 25, no. 12, pp. 1547–1564, Dec. 2006.

[10] K. S. Ambrosen *et al.*, "Validation of structural brain connectivity networks: The impact of scanning parameters," *Neuroimage*, vol. 204, p. 116207, Jan. 2020.

[11] K. H. Maier-Hein *et al.*, "The challenge of mapping the human connectome based on diffusion tractography," *Nat. Commun.*, vol. 8, no. 1, p. 1349, Nov. 2017.

[12] P. M. Thompson *et al.*, "ENIGMA and global neuroscience: A decade of large-scale studies of the brain in health and disease across more than 40 countries," *Transl. Psychiatry*, vol. 10, no. 1, p. 100, Mar. 2020.

[13] S. M. Smith *et al.*, "Tract-based spatial statistics: voxelwise analysis of multi-subject diffusion data," *Neuroimage*, vol. 31, no. 4, pp. 1487–1505, Jul. 2006.

[14] N. Jahanshad *et al.*, "Multi-site genetic analysis of diffusion images and voxelwise heritability analysis: a pilot project of the ENIGMA-DTI working group," *Neuroimage*, vol. 81, pp. 455–469, Nov. 2013.

[15] J. B. Colby, L. Soderberg, C. Lebel, I. D. Dinov, P. M. Thompson, and E. R. Sowell, "Along-tract statistics allow for enhanced tractography analysis," *Neuroimage*, vol. 59, no. 4, pp. 3227–3242, Feb. 2012.

[16] C. Sullivan and A. Kaszynski, "PyVista: 3D plotting and mesh analysis through a streamlined interface for the Visualization Toolkit (VTK)," *J. Open Source Softw.*, vol. 4, no. 37, p. 1450, May 2019.

[17] W. Schroeder, K. Martin, and B. Lorensen, *The Visualization Toolkit: An Object-oriented Approach to 3D Graphics*. Kitware, 2006.

[18] D. C. Van Essen *et al.*, "The WU-Minn Human Connectome Project: an overview," *Neuroimage*, vol. 80, pp. 62–79, Oct. 2013.

[19] M. Paquette, G. Gilbert, and M. Descoteaux, *Penthera 3T*. 2019.

[20] J. V. Manjón, P. Coupé, L. Concha, A. Buades, D. L. Collins, and M. Robles, "Diffusion weighted image denoising using overcomplete local PCA," *PLoS One*, vol. 8, no. 9, p. e73021, Sep. 2013.

[21] [1] E. Kellner, B. Dhital, V. G. Kiselev, and M. Reisert, "Gibbs-ringing artifact removal based on local subvoxel-shifts," *Magn. Reson. Med.*, vol. 76, no. 5, pp. 1574–1581, Nov. 2016.

[22] J. L. R. Andersson and S. N. Sotiropoulos, "An integrated approach to correction for off-resonance effects and subject movement in diffusion MR imaging," *Neuroimage*, vol. 125, pp. 1063–1078, Jan. 2016.

[23] B. Jeurissen, J.-D. Tournier, T. Dhollander, A. Connelly, and J. Sijbers, "Multi-tissue constrained spherical deconvolution for improved analysis of multi-shell diffusion MRI data," Neuroimage, vol. 103, pp. 411–426, Dec. 2014.

[24] R. Vallat, "Pingouin: statistics in Python," *J. Open Source Softw.*, vol. 3, no. 31, p. 1026, Nov. 2018.

[25] P. E. Shrout and J. L. Fleiss, "Intraclass correlations: uses in assessing rater reliability," *Psychol. Bull.*, vol. 86, no. 2, pp. 420–428, Mar. 1979.

[26] A. Zavaliangos-Petropulu *et al.*, "Diffusion MRI Indices and Their Relation to Cognitive Impairment in Brain Aging: The Updated Multi-protocol Approach in ADNI3," *Front. Neuroinform.*, vol. 13, p. 2, Feb. 2019.

[27] C. R. Jack Jr *et al.*, "Defining imaging biomarker cut points for brain aging and Alzheimer's disease," *Alzheimers. Dement.*, vol. 13, no. 3, pp. 205–216, Mar. 2017.